A High-Speed Chip-Scale Rotary Polygon Optical Scanner Based on a Micromotor Integrated With a Micro-Polyhedron Mirror

Amit Gour , *Member, IEEE*, Michaël Ménard, *Member, IEEE*, and Frederic Nabki , *Member, IEEE*

Abstract—Micro-opto-electro-mechanical systems (MOEMS) based mirrors with a suitable actuation range are often used for optical beam scanning applications. While several MOEMS scanners have been reported, they often have limitations with respect to their range of motion, field of view, mass, size and fabrication cost. In this work, we present a rotary micro-polygon scanner based on an electrostatic variable capacitance micromotor for laser beam steering applications. The miniaturized scanner consists of a hollow micro-polyhedron mirror with a base radius of 200 μm and a height of 400 μm. It is mounted on the rotor of a variable capacitance micromotor using an epoxy-based adhesive. The rotor has a diameter of 600 μm and is 2.5 μm thick. The micromotor was fabricated using a commercial three-layer polysilicon surface micro-machining process (PolyMUMPs) and the micro-polyhedrons were fabricated using a commercial bulk micro-machining process (PiezeoMUMPs). After fabrication of the components, the micro-scanner was assembled and operated under atmospheric conditions using a three-phase square wave excitation ranging from 0 V to 200 V and achieved rotational speeds of up to 2100 rpm. An optical laser beam with a wavelength of 632 nm was reflected off the sidewall of the rotating micro-polyhedron, achieving an experimentally measured scanning angular range of 57.88°, an angular scan rate of 220 radians per second and a scan speed of 25,200 lines per minute or 420 lines per second with a 12 sided micro-mirror. The ratio of the output power over the input optical power is measured over a scanning range of 22°, which is limited by the size of the photo-detector, yielding a ratio spanning from 0.18 to 0.22. This rotary micro-scanner can provide high scanning speeds and a wide scanning field of view with a footprint of 1.25 mm² and a thickness of 0.83 mm, which is suitable to implement chip-level high-performance micro-beam steering systems for various applications. **[2022-0020]**

Index Terms—Variable capacitance micromotor, rotary polyhedron scanner, micro-assembly, adhesive bonding, chip-scale integration.

I. INTRODUCTION

OPTICAL scanning is used in a wide range of applications including telecommunications, barcode readers, light detection and ranging (LiDAR) systems, optical imaging systems, optical displays, optical switches and laser printers [1]. Optical scanners with compact size, fast beam scanning and high resolution are required to push the boundaries of such applications. Polygon scanners [2], acousto-optic scanners [3], Risley-prism scanners [4] and galvanometric scanners [5] are common techniques for laser beam scanning. Recently, LiDAR has gained popularity due to its application in autonomous cars and other unmanned vehicles where it acts as a core technology for remote sensing and environment monitoring [6]–[10]. Advanced driver assistance systems [7] based on LiDAR are required to cover a wide range of specifications, including wide or narrow fields of view (FoV), high scan rate, and long or short operating range. Typically, commercial LiDARs use a rotating mirror or a polygon scanner [9], [11]–[14] actuated by an electric motor for beam scanning, resulting in a large system. Nevertheless, these devices provide a wide FoV with straight and parallel scan lines having a uniform speed, making them highly popular scanning solutions for LiDAR sensors. The scanning mechanism used in a LiDAR system is a key parameter to determine its overall size, mass and power consumption. LiDARs with a rotating scanner configuration can achieve the performance required but are bulky and expensive. Moreover, when these scanning systems are installed on a vehicle, they often disrupt the vehicle design, which is a major drawback for commercialization. Thus, a compact, i.e. match-box sized, affordable and reliable scanning unit for large-scale applications is needed and its development presents a significant challenge.

Scanners based on non-mechanical structures such as acousto-optic scanners employ refraction or diffraction to redirect the laser beam. They offer high scanning speeds but provide only a small angular range compared to mirror scanners. They also suffer from high optical power losses. For instance, miniaturized and monolithic scanners using an optical phase array (OPA) can be implemented using silicon photonics that can deliver wide scanning angle at low operating voltage [15]. However, the technology readiness level of OPA-based LiDAR scanners is low due to several design trade-offs such as light source integration, grating coupler

design, integration with driving electronics and thermal management [16]. Galvanometric scanners are widely used in laser displays and confocal microscopy due to their high speed, accurate movement, and good scanning resolution. However, to operate along two axes, they need two separate scanners mounted perpendicularly, resulting in a device that is too bulky for portable systems [17]. Also, galvanometric scanners are unable to provide a linear scan rate due to the oscillatory motion of the resonant mirror, limiting their applications to high-speed raster scanning systems [18].

High-speed optical scanners are also realized by using rotating mirrors based on motors [1]. These scanners consist of a polygon shaped mirror mounted on a motor to deflect the incoming laser beam, and hence generate a line scan. The rotational motion of the polygon scanner provides a constant angular scan rate and fast scanning speed making it a key element in many applications such as digital scanners, laser printers, barcode readers and swept-source lasers [19]–[22]. A high scanning frequency can be obtained at the expense of the scan angle with polygon scanners by increasing the number of facets of the polygon mirror, resulting in record-breaking image acquisition rates for optical coherence tomography and confocal microscopy [23]. Rotating mirror scanners are also used in LiDAR systems due to their ability to provide a wide FoV, but these polygon scanners suffer from high power consumption and have a large footprint [24]. However, they are widely used in commercial laser scanners since they have shown the largest maximum deflection angles and the fastest angular speeds to date.

With the advent of applications requiring environment monitoring, such as surveillance drones, self-driving cars, and autonomous underwater vehicles, there are tremendous efforts to realize miniaturized scanning systems. Large-scale deployment of these systems requires scanner modules that are smaller and more efficient than macro-optical systems. Accordingly, LiDAR scaling can be achieved by using a scanning mechanism based on micro-electromechanical systems (MEMS) technology. Scanning or switching mirrors based on MEMS actuators can reduce the size and cost of scanning systems [25]. There are a variety of MEMS scanners that have built-in electrostatic actuation, external magnetic actuation or external galvanic actuation [26]. The latter provides large scan angles by using two single-axis mirrors for 2D scanning but makes the system rather large. Moreover, galvanometric MEMS mirrors are resonant devices, and thus are operated at their resonant frequency, providing non-uniform speed and non-linear resolution. Optical scanners based on a translating curved mirror can offer a wide scanning range and uniform spot size as they can avoid the dynamic bending of the micromirror, which is a significant issue in torsional scanners. Reflection-based translating curved mirrors have been reported to achieve a scanning range of up-to 110 ° [27]. However, they use comb drive actuators for translational motion, making them a resonant scanner, thus unable to produce a uniform scanning resolution. On the other hand, scanners based on refraction using a translational micro-lens are non-resonant and operate using scratch drive actuators, but provide a very small scanning range of ± 7 ° [28]. On the other hand, polygon scanners operate at a constant speed offering a uniform scan rate, have a wide scanning range and better resolution than galvanometric and resonant mirrors. Thus, a MEMS based rotary polygon scanner offers a great alternative to exploit the fabrication benefits of MEMS technology and the scanning performance of polygon scanners.

A small footprint, light weight, low power consumption and low-cost due to batch-fabrication are a few of the benefits of MEMS-based optical scanners. Nonetheless, the implementation of a rotary polygon scanner using MEMS technology that is capable of full revolutions is challenging. The choice of the actuation mechanism, the development of the fabrication process and of the micro-assembly procedures are the key challenges for achieving a MEMS optical scanner. Several micro-assembly mechanisms and post-processing techniques have been developed to manipulate surface micro-machined 2-D micro-structures to construct 3-D, out-of-plane MEMS devices. In [29], a MEMS scanner for optical switching applications was designed and fabricated to achieve a large angular displacement. The scanner was fabricated using the SOIMUMPS process and was able to rotate by $\pm 8.5°$ in the X-Y plane at 290 V. A MEMS rotating polygon micromirror with six facets based on a outer-rotor wobble micromotor was fabricated using a silicon-on-insulator (SOI) wafer [30]. The rotor diameter was 1.4 mm and flew away when rotating at high speeds, thereby limiting the maximum operational speed to only 58 rpm. In [31], deflecting flexible structures employing analog controls are reported to rotate micro-mirrors but the rotation angle of the micro-mirrors was limited to 1.5 °. In [32] a 3D rotating polygon scanner was constructed by assembling a micromirror on top of a variable capacitance micromotor using robotic micro-manipulators. A specially designed micromirror compatible with a variable capacitance micromotor was used to facilitate the assembly and was fabricated using the PolyMUMPS process. However, no rotation of the assembled scanner was reported. Therefore, developing a rotary micro-scanner based on MEMS technology remains challenging and requires solutions to a multitude of technical difficulties.

Accordingly, in this work, a rotary chip-scale micro-polygon scanner with a 12 sided micromirror is designed, fabricated, assembled and tested. The size of the micro-scanner is 1 mm × 1 mm × 1 mm and it is capable of 25,200 line-scans per minute while covering an angular range of 57.88°. This integrated beam steering system consists of a movable high-aspect ratio micro-polyhedron mirror that is rotated by a micromotor. It interacts with a laser beam propagating parallel to the surface of the substrate. Traditional surface-micromachining technology produces planar films with thickness on the order of a few microns, which is very small compared to the diameter of a collimated laser beam. Thus, extra processing steps are required to make a three-dimensional structure with a height suitable to steer a laser beam. Therefore, additional components and space are required for precise alignment, increasing the challenges and complexity of scanner miniaturization. The assembled 3D micro-polygon scanner presented here is suitable for scanning applications requiring a wide FoV, small footprint, and low
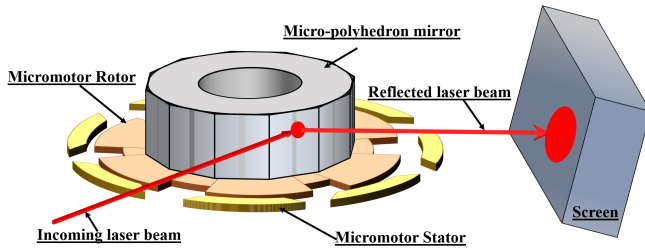
Fig. 1. Diagram illustrating the rotary micro-scanner.

Fig. 2. Diagram showing the various parts of the micromotor: a) top-view, and b) cross-section.

power consumption. Also, the output power of the reflected beam for potential optical switching or attenuation applications is estimated.

An overview of the rotary micro-polygon scanner is presented in Section II, along with details pertaining to the design of its components (i.e., micro-polyhedron mirror and micromotor). Section III overviews the fabrication of the components and the micro-assembly process. Section IV discusses the results of the electrical and optical characterizations of the device and is followed by a discussion.

II. ROTARY MICRO-POLYGON SCANNER DESIGN

A. System Overview

The various parts of the micro rotary scanner (μRS) are shown in Figure 1 and consist of a micropolyhedron mirror (μPM) attached to the rotor of a micromotor. The μPM can rotate at a constant speed and perform optical line scanning. The μPM is attached to the micromotor using micro-assembly. The angular scan range and the scan line rate can be tuned by using a μPM with a suitable number of sides for the target application. The μPM has smooth sidewalls resulting in specular reflection of the incident laser beam and the reflected beam is imaged on a screen for demonstration purposes in this work. A three-phase variable capacitance micromotor (VCM) based on electrostatic actuation is used as the rotary platform and is capable of rotating at high speed with low power consumption. When the μPM starts rotating, a line scan of the reflected laser beam is observable on the screen. The frequency of the actuation signal of the micromotor determines the rotational speed of the μPM. Accordingly, the rate of the generated scan lines varies with the frequency of the excitation signal. The chip-scale implementation of the μRS demonstrated here involves: i) the design and fabrication of a chip-scale rotary platform; ii) the design and fabrication of a μPM that can be attached to the rotary platform; and iii) a micro-assembly technique to integrate the μPM with the rotary platform (i.e. the micromotor).

B. Micromotor Design

The requirements on the rotary platform for the implementation of the chip-scale μRS are: i) dimensions on the order of 100's of microns; ii) the ability to perform complete revolutions at high speed; and iii) a reliable fabrication process, preferably with commercial batch fabrication to minimize cost. VCMs are small, can rotate at high speeds, and
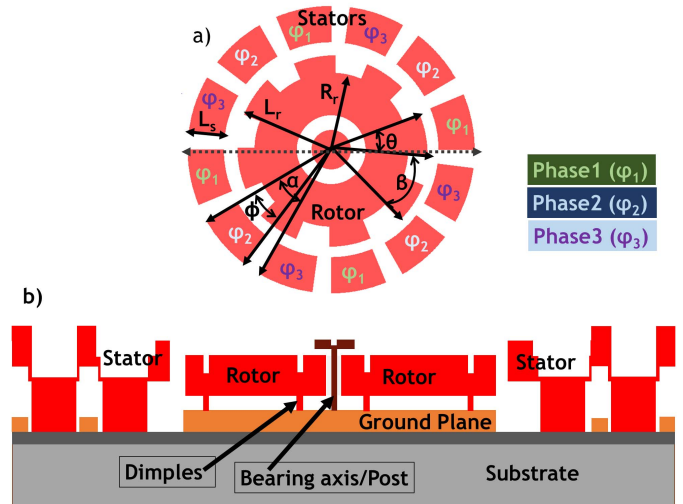
can be fabricated using surface micromachining processes, making them an ideal choice for implementing the rotary platform. Many types of electrostatic side drive micromotors were implemented in the past using surface micromachining processes. Often, the micromotor fabrication process is developed in-house and this makes the reproducibility of the device challenging. Thus, it is preferable to adopt a standard commercial fabrication process. The PolyMUMPS process is a two-layer polysilicon micromachining process widely used in both the industry and academia to implement various MEMS devices. The rotational motion of the μRS is governed by the motion of the micromotor. Thus, the design of a micromotor with high torque and high-speed rotary motion using a commercial process is vital to this work, and has been inspired from [33] in order to fabricate chip-scale micromotors for the μRS. We implemented high-speed VCM architectures [33] using the PolyMUMPS process that can rotate at up to 8,000 rpm without loading, i.e. without any component attached to the rotor, and we used them to implement the μRS. Figure 2 shows the various parts of a variable capacitance micromotor, and the key geometrical parameters optimized for torque enhancement based on analytical modelling [33], [34]. The VCM used here consists of 8 rotor poles and 12 stator poles, the radius of the rotor is 300 μm, the bearing axis/post has a radius of 6 μm, and the dimples have a radius of 3 μm. The bearing post/axis is the axis of rotation of the rotor, and it also prevents rotor-stator collisions. The dimples are part of the rotor, and provide electrical contact to the underlying ground plane and stability while rotating. The design parameters of the VCM are listed in Table I.

When the rotor is grounded and a voltage is applied to the stator poles, an electrostatic force is generated between the stator poles and the rotor poles. The tangential component of the electrostatic force moves the rotor and complete rotations are achieved by applying a three-phase varying voltage to the stator poles. The movement of the rotor changes the overlap

TABLE I

VCM DESIGN PARAMETERS

Geometrical parameters	Value
Number of phases (q)	3
Total number of stator poles (N$_s$)	12
Total number of rotor poles (N$_r$)	8
Radius of the micromotor rotor (R$_r$)	300μm
Gap between rotor and stator (G)	2.5 μm
Length of the stator tooth (L$_s$)	140 μm
Length of the rotor tooth (L$_r$)	417.75 μm
Number of dimples	4
Radius of the bearing axis	3 μm
Stator angular pitch (α) and angular width (ϕ)	22.5°, 30°
Rotor angular pitch (β) and angular width (θ)	22.5°, 45°

area between the rotor poles and the stator poles, thereby modifying the capacitance between the rotor and the stator poles. The torque acting on the rotor is proportional to the change in the rotor-stator capacitance (C) with respect to the angular position of the rotor (Ω), applied voltage (V), frequency of excitation (f_{ele}), total number of stator poles (N_e), total number of rotor poles (N_r) and the number of voltage phases (q). The derived motive torque per phase and the rotational speed is given by [33], [35], [36]:

$$T(\Omega) = \frac{N_e V^2}{2q}\left(\frac{dC(\Omega)}{d\Omega}\right) \qquad (1)$$

$$\omega_r = 60\frac{f_{ele}}{N_r} \quad rpm \qquad (2)$$

The number of rotor poles of the micromotor depends on the stator pole and the ratio of total number of stator poles to the total number of stator poles is 1.5 for maximum torque [33], [34]. Accordingly, a VCM with a large number of poles is slow, and has high torque. In contrast, a VCM with a small number of poles is fast, but is unable to produce a high torque. Here, the VCM is optimized to provide sufficient torque while providing rapid motion when loaded with the μPM element, resulting in a fast scanning chip-scale device. The lifespan of the μRS is dependent on the wear due to the friction of the various parts of the micromotor. Friction in the micromotor exists between the rotor and the central pin bearing, and between the dimple and the ground plane. The friction can be minimized by having less dimples and minimizing their size, and by using a smaller central pin bearing [37], [38]. These techniques were implemented in the micromotor design proposed by choosing bushing type dimples with a diameter of 6μm and a central pin bearing having a diameter of 12μm [33]. Another factor that impacts friction is the clearance of the central pin bearing around the rotor, which should minimized [39]. This is determined by the fabrication process and, for the PolyMUMPS process, is limited to 750 nm [40].

C. Micro-Polyhedron Mirror Design

The μPM used in the implementation of the μRS should be light weight and have smooth and sufficiently large facets to reflect the incident laser beam. The maximum possible size of the base of the μPM is determined by the diameter of the rotor, and in our case, it must be less than 600 μm. A contact between the μPM and stator poles can also lead to device failure by causing a short-circuit. Thus, it is important to ensure the proper placement of the μPM onto the rotor and prohibit any overhang outside of the rotor that may damage the stator poles. Any damage to the bearing post/axis located at the center of the VCM as shown in Figure 2 results in the failure of the micromotor. Thus, the geometry of the μPM must be designed to never touch the bearing post/axis. This design constraint is necessary to ensure proper operation of the rotor and requires a recess at the center of the μPM. The dimension of the recess must be greater than the dimension of the bearing axis, which has a height of 1.5 μm and a diameter of 12 μm.

The facets of the μPM are acting as mirrors to reflect an incoming laser beam, and thus they must have a sufficiently large area to deflect the entire incoming beam. The number of sides of the μPM determines the angular range of the scanner and the scan line rate. More sides increases the line rate but decreases the angular range, therefore the shape of the μPM should be chosen according to the targeted application. Additionally, the maximum number of side-wall mirrors of the μPM are limited by its size, since as the number of sides increases, the area of each facet decreases, which could ultimately lead to significant optical losses. Here, we chose a μPM with 12 sides for demonstration purposes since it offers the best trade-off between the compatibility of the facet size with our optical test setup and the maximum scan speed that can be demonstrated. The height of the μPM should be large enough to accommodate the beam spot size without any distortion. However, a μPM with large height can result in a bulky structure that may induce stress in the thin rotor film. Thus, the choice of the μPM dimensions depends on the micromotor and the requirements of the target application. Accordingly, the design constraints on the μPM includes a recess at the centre with a size greater than the dimensions of the bearing post/axis, and a μPM base size of less than 600 μm. Moreover, there is a trade-off between the angular range, line scan rate and facet size when choosing the number of sides of the μPM.

The final prototypes of the μPM were fabricated using the commercial PiezoMUMPs process. This process leverages deep reactive ion etching (DRIE) to create steep sidewalls and trenches in a silicon-on-insulator wafer, making it a suitable fabrication technique to implement the μPM structure having a height equal to the depth of the trench which is derived from the substrate thickness (i.e., 400 μm). Also, the process uses a silicon device layer with a thickness of 10 μm on top of the substrate that enables the creation of a recess with the required dimensions. The chip layout of various μPMs designed to meet these constraints are shown in Figure 3(a). A single μPM design consists of a trench region, a micro-polyhedron
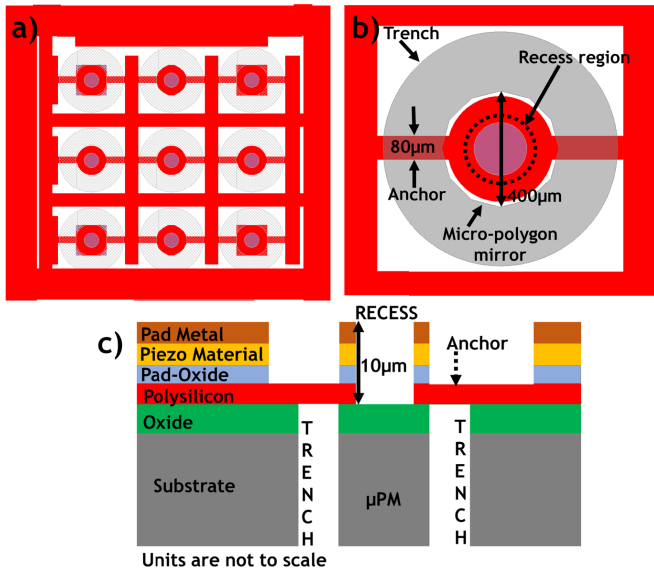
Fig. 3. a) Image showing the layout of the micro-polyhedron chip; b) image of the layout showing the parts of a single μPM design; and c) cross-sectional view of the micro-polyhedron design implemented with the PizeoMUMPs process.

Fig. 4. SEM micrograph of the micromotor fabricated using the PolyMUMPs surface micromachining process.

mirror, a recess region, and two anchors to support the mirror structure, as shown in Figure 3(b), and the corresponding cross-section is illustrated in Figure 3(c). A circular region at the centre of the μPM, where the recess region must be present is also shown in Figure 3(c). The dimensions of the recess are chosen to allow easy placement of the μPM onto the rotor of the VCM, while avoiding any contact and damage to the bearing axis.

III. DEVICE FABRICATION AND ASSEMBLY

A. Micromotor Fabrication

The VCM was fabricated using the PolyMUMPs surface micromachining process [40] and a scanning electron microscope (SEM) micrograph of the device is shown in Figure 4. Optical imaging is used to verify that there are no joints or contacts between the rotor and stator poles. In addition, the interconnects connecting the input pads to the micromotor poles are electrically tested to identify short or open connections. The rotor acts as the rotary platform, and its free movement is verified by pushing it using micro-probes without any excitation. This ensures that the rotor is fully released and capable of motion without adhering to the substrate or the bearing axis. Various designs of VCMs were tested without micro-polyhedron mirrors, as reported in [33], and most of the designs were readily able to achieve rotational speeds greater than 2000 rpm. Also, a specific VCM design with a stator to rotor gap of 2 μm can provide maximum speeds of up to 7,875 rpm. It was observed that a few devices having stator to rotor gaps of 2 μm suffered from incomplete etching of the gap making a connection between the rotor poles and the stator poles, precluding from correct operation. Consequently to avoid this issue, in this work, a VCM with a stator to rotor gap of 2.5 μm was used.
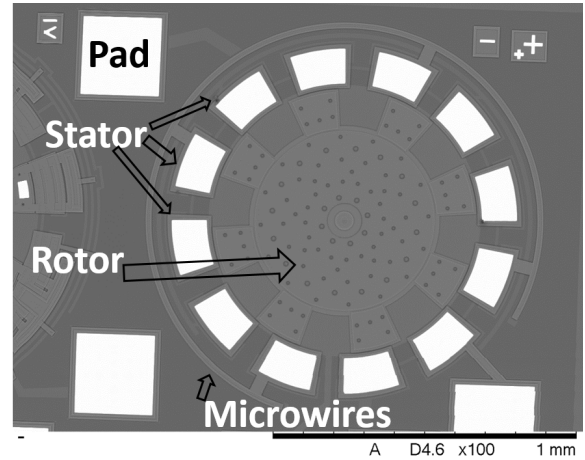
B. Micro-Polyhedron Mirror Fabrication

Micro-polyhedrons with 4, 8 and 12 sides were fabricated using the PiezoMUMPs bulk micromachining process [41], and a μPM with 12 sides was selected to implement the μRS presented in this work. Images of the top and bottom of the μPMs are shown in Figure 5. The μPMs are obtained from the DRIE of the backside of the silicon wafer, creating high aspect ratio sidewalls suitable to act as mirrors to deflect a laser beam. However, the sidewalls obtained with the PiezoMUMPS process have low reflectance and low flatness due to DRIE-induced scalloping on the surface [38], [42]. Nevertheless, the DRIE process could be optimized to produce etched surfaces with suitable optical properties [43], [44], resulting in a μPM with high reflectivity. This will be discussed further in the Experimental Results section. Moreover, the μPMs are firmly attached to the die with thin anchors or teethers in the silicon device layer, as shown in Figure 5(a). These can be easily broken with a micro-probe to release the μPM. This significantly facilitates the handling and manipulation of the μPMs during the micro-assembly operation. The released μPM can be cleaned using sonication in an inert solvent followed by rinsing using nitrogen to remove particles that may be present on it after the anchors are broken. The DRIE step of the PizeoMUMPs process allows the formation of large trenches on the backside of the substrate but it is impossible to make a small recess inside the μPM from the back. A small recess is required to ensure that the μPM never touches the bearing post/axis of the VCM. Thus, a central recess in the μPM is created by etching the device layer, as illustrated in Figure 5(b). The diameter of the circular recess is 100 μm, which is sufficiently large to keep the edges of the μPM away from the bearing post/axis of the VCM after the micro-assembly process. Moreover, the depth of the recess is 10 μm, which is greater than the height of the VCM bearing post/axis to avoid any vertical contact. As apparent in Figures 5(c) and 5(d), the μPM is relatively thick. It has a thickness of 400 μm, a base radius of 200 μm, and each of the 12 sides of the polyhedron are 100 μm long. The resulting silicon μPM has a mass of approximately 123 μg.
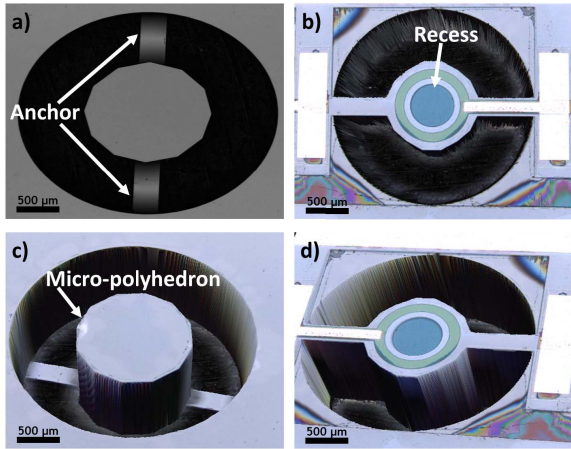
Fig. 5. Images of the micro-polyhedron fabricated using the PizeoMUMPs bulk micromachining process: a) top view of the bottom side of the micro-polyhedron; b) top view of the top-side; c) isometric view from the bottom; and d) isometric view from the top.

C. Assembly of the Rotary Polygon Scanner

Serial micro-assembly was performed to integrate the μPM with the VCM to achieve the μRS. Often, specially designed structures need to be added to MEMS devices to perform 3D micro-assembly, which may add complexity to the integration operation. Here, a simple protocol was developed to integrate the μPM to the VCM rotor in order to simplify the micro-assembly. The protocol involves the deposition of a bonding material onto the μPM, placing the μPM onto the rotary platform and finally bonding the μPM with the rotor using thermal curing. Figure 6 shows the various steps involved in the micro-assembly of the μPM on the rotor.

A SU-8 based adhesive is used to bond the μPM to the rotor. SU-8 is an epoxy based negative photo-resist that is commonly used for adhesive bonding with and without UV curing [45]. Here, bonding is performed by thermal curing of the SU-8. The advantage of using SU-8 is that it can rapidly change it physical state from a glue-like semi-solid phase to a solid phase and vice-versa at low temperature. The base of the μPM is not as wide as the diameter of the rotor of the VCM, but it is large enough to deposit droplets of adhesive. The following procedure is employed to deposit a solid SU-8 adhesive layer onto the μPM. First, droplets of SU-8 are deposited onto the μPM by drop-casting and heated to 50°C for 2 minutes, 60°C for 2 minutes and 90°C for 2 minutes in order to vaporize the solvent. Then, the μPM with SU-8 drops is cooled down at room temperature for 30 minutes to solidify the adhesive drops.

A single MEMS chip consists of several VCMs, and to precisely place a μPM on a particular VCM without damaging or touching the other devices is challenging. Therefore, a pick and place technique using a placement mask was developed to position the μPM onto the rotor of the VCM. The placement mask was made from a 90 μm thick rigid steel composite sheet into which holes with a diameter equal to that of the base of the μPM were drilled using laser ablation. The purpose of this mask is to allow obstacle-free navigation of the μPM

over the MEMS chip and to position it into a hole that is aligned to the rotor of the VCM. The MEMS chip was placed between two support posts such that the height of the support posts is slightly greater than the MEMS chip by approximately 20-50 μm. Accordingly, when the placement mask is aligned with the rotor and placed onto the support posts, it does not touch the MEMS chip as the extra height of the support posts creates a gap between the chip and the placement mask, preventing damage to the devices during the micro-assembly. The key for controlling the gap between the alignment plate (i.e., placement mask) and the MEMS chip is the support post. The height of the support post is greater than the height of the MEMS chip such that when the alignment plate is placed on these posts, a cavity with the desired gap is obtained. The support post can be made by stacking glass slides, square shape pieces of silicon wafers or any desired material with the proper thickness to obtain the required gap. Here, we have used rectangular shape plastic plates as a support post. The arrangement of the MEMS chip with the support post is attached to a glass slide using double sided scotch tape making a robust platform for handling and alignment.

The micro-positioners can move the placement mask with 25 μm accuracy along each axis. The placement mask was aligned and placed over the rotor of the VCM using micro-positioners, as shown in Figure 7. A μPM with solidified adhesive was picked and placed onto the placement mask using plastic tweezers and pushed into the alignment hole using micro-probes. The μPM cannot drop, fall or topple from the rotor after being inserted into the alignment hole since the thickness of the μPM is greater than that of the placement mask and gap combined.

After positioning the μPM onto the rotor of the VCM, the placement mask is removed and the assembled components are heated at 90°C for 2 minutes to reflow the SU-8. It is then cooled down to room temperature for 45 minutes to bond the μPM to the rotor.

SEM micrographs of the assembled μRS are shown in Figure 8.

IV. EXPERIMENTAL RESULTS

The characterization of the μRS was carried-out by activating the micromotor and focusing a laser beam onto the sidewalls of the rotating μPM. A block diagram of the experimental setup is shown in Figure 9(a). A DC-signal is amplified and supplied to a three-phase square wave generator to actuate the micromotor. The light from a 632 nm HeNe laser (OFV-534 from Polytec) is focused onto the sidewall of the μPM. The laser power is less than 1 mW and the laser head optics can focus the beam down to a spot size of 1.5 μm using a 20X objective or 5 μm using a 5X objective. The collimator on the laser head can be adjusted to modify the spot size and a screen is placed near the edge of the chip to visualize the reflected signal. The maximum three-phase input voltage to the micromotor is limited to 200 V peak-to-peak in order to avoid dielectric breakdown in the gap between the rotor and the stator. After the optical alignment of the laser beam, the
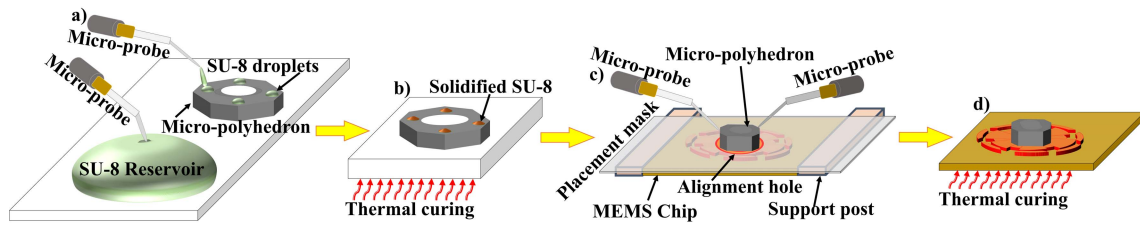
Fig. 6. Diagram showing the steps involved in the micro-assembly technique to integrate the micro-polyhedron onto the micromotor: a) drop-casting of SU-8 droplets onto the micro-polyhedron; b) thermal curing of the micro-polyhedron to solidify the SU-8 droplets; c) alignment and placement of the micro-polyhedron with solidified SU-8 droplets on to the micromotor; and d) final thermal curing of the assembled micro-components to bond the micro-polyhedron with the micromotor.
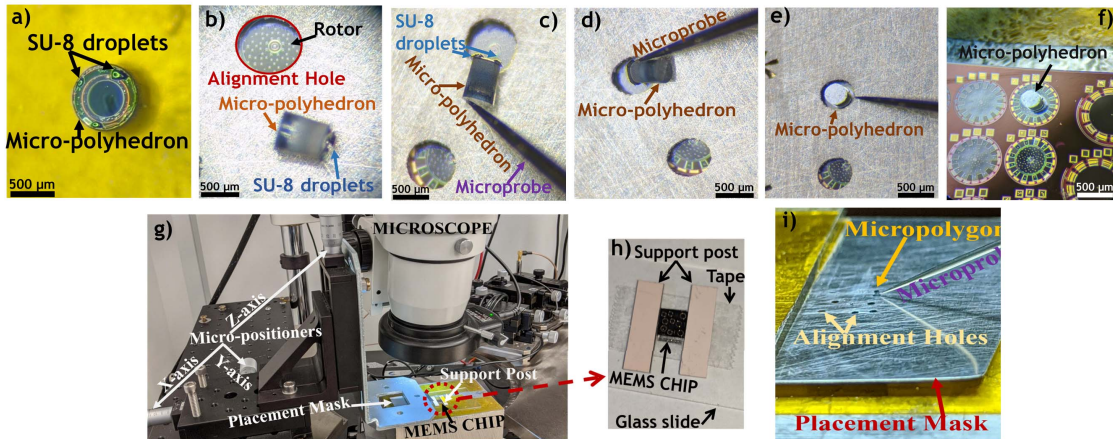

Fig. 7. Images of different steps performed during the micro-assembly process: a) solidified SU-8 drop on the micro-polyhedron; b)–e) images showing the placement of the micro-polyhedron onto the rotor via an alignment hole using micro-probes; f) assembled micro-scanner; g) setup used for the micro-assembly; h) setup used for holding the MEMS die and alignment; and i) alignment holes on the placement mask and the placed micro-polyhedron.
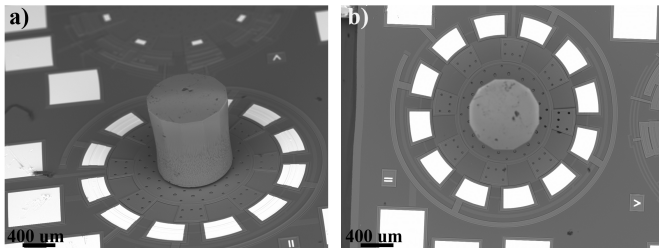

Fig. 8. SEM micrographs of the assembled micro rotary scanner: a) isometric view of the micro-polyhedron on the micromotor; and b) top view of the micro-polyhedron on the micromotor.

actuating three-phase signal is applied, and a CCD mounted onto the microscope captures the scanner motion and the beam position on the screen. The laser head also has a camera that captures a side-view of the polyhedron mirror as shown in Figure 9(c). A simplified top-view of the system, including the chip housing the μRS, is shown in Figure 9(b).

The voltages at which the μPM rotates and the maximum frequency that can be applied at those voltages was characterized to determine the mechanical performance of the μRS. The following experimental procedure was used for the electrical characterization of the μRS, which started at an input voltage of 0 V: i) the input voltage was increased in steps of 2 V while keeping the three-phase signal frequency at 10 Hz until the VCM started rotating; ii) the input frequency was

then increased in steps of 10 Hz while keeping the voltage obtained in the previous step constant until the VCM stopped rotating; iii) Steps i and ii were repeated until the input voltage reached 200 V.

However, the μPM remained motionless irrespective of the applied excitation during the initial testing. The 0.5 μg rotor is a 2 μm thick layer supported by four dimples having a diameter of 6 μm and a height of 750 nm. A low number of dimples were used to minimize friction of the rotor during the rotation. It was expected that the mirror would move at a high input voltage since the VCM torque is proportional to the applied voltage. Nevertheless, it was noticed that the increase in the inertial mass of the rotor due to the loading of the μPM had significantly increased the static friction of the rotor, precluding the startup of the VCM. The rotational inertia, assuming the geometry of the μPM as a cylinder, the rotor as a disc and considering the density of the silicon wafer as 2330 kg/m^3 is 2.53×10^{-10} kg/m^2. Therefore, the mass of the loaded rotor (i.e., with a micro-polyhedron having mass of 123 μg) considerably increases the inertia, and as a result, it is not able to start rotating when a voltage is applied.

A. Micro-Polyhedron Mirror Mass Reduction

As mentioned in the previous section, modifications to lighten the μPM were required to enable the rotary motion
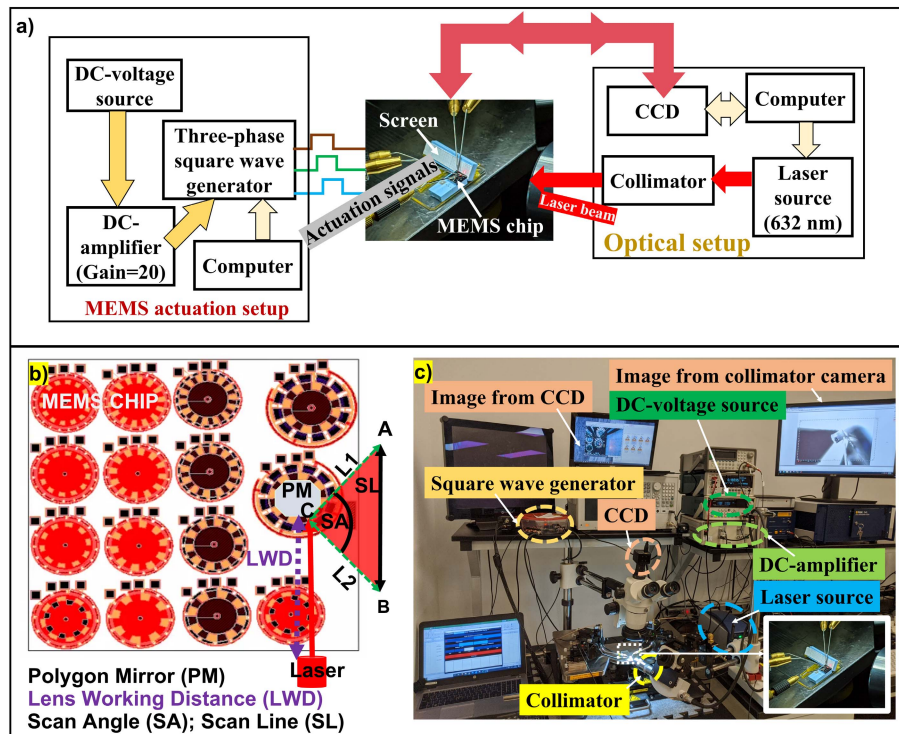
Fig. 9. a) Block diagram showing the experimental setup required for micromotor actuation and optical characterization; b) diagram depicting the chip housing the μRS, which also includes different VCM designs, along with the incident laser beam and reflected beam; and c) image showing all of the instruments used in the characterization.

of the μRS. The dimensions of the μPM were chosen to ensure that it is sufficiently high and wide to reflect the laser beam entirely in order to minimize optical losses. When reducing its mass, the dimensions of the side-walls should not be modified to avoid compromising its optical characteristics. Accordingly, this issue was resolved by drilling a hole through the center of the μPM using laser ablation to reduce its mass, while maintaining the optical requirements. The laser ablation technique is simple, fast, and capable of precisely removing the unnecessary mass from the desired location on the μPM structure. A LPKF ProtoLaser U3 tool is used for laser ablation with the following process parameters: a laser power of 6 W with a pulse repetition rate of 40 kHz. The precision of the laser ablation system is 50 μm, thus it can easily ablate the materials with dimensions greater than 50 μm. The laser source has a wavelength of 355 nm and a feedrate of about 3.54 mil per minute to drill a hole of 250 um in diameter into the micro-polyhedron. A SEM micrograph of the laser ablated μPM is shown in Figure 10(a). As can be seen, a cylinder having a diameter of 250 μm and centered within the μPM was removed by laser ablation. The ablated μPM has an estimated mass of 75 μg, which is 39% less than the original structure. Also, the rotational inertia after the laser ablation is 1.59×10^{-15} kg/m^2, which is an improvement of approximately 37%. This method allowed to remove a significant portion of the mass without compromising the functionality of the μPM. The ablated μPM is attached to the micromotor using the same micro-assembly technique previously presented. SEM micrographs of the assembled system
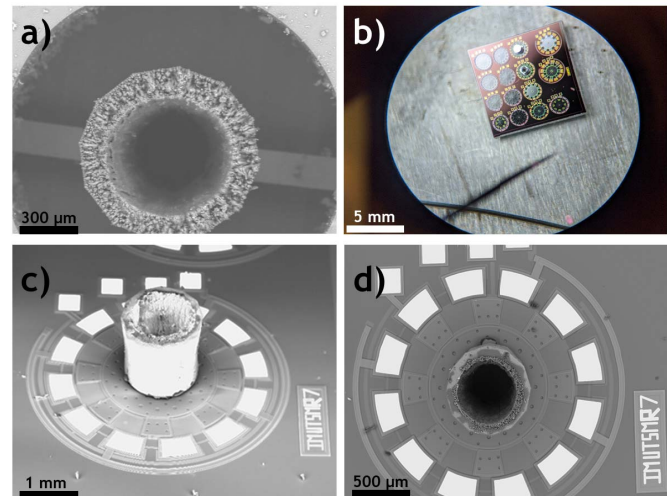

Fig. 10. a) SEM micrograph of the laser ablated μPM; b) microscopic image of the assembled micro rotary scanner; c) SEM micrograph showing an isometric view of the micro rotary scanner; and d) SEM micrograph showing the top-view of the micro rotary scanner.

are shown in Figures 10(b)-(d). With the aforementioned modification to the μPM, the device was able to operate as a results of the reduced mass.

B. Electrical Characterization

The electrical characterization of the μRS was performed to measure its power consumption, rotational speed, and actua-
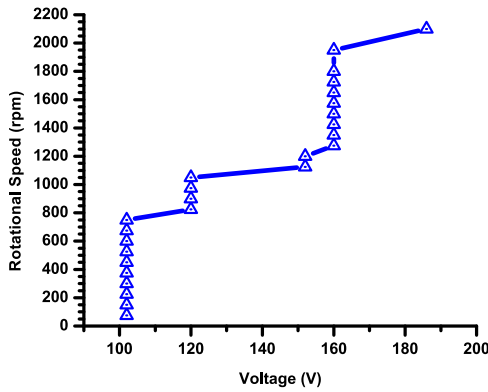
Fig. 11.   Calculated rotational speed of the micro rotary scanner vs. the amplitude of the applied three-phase driving voltage.

Fig. 12.   Measured electrical power consumption vs. rotational speed for the micro rotary scanner and the unloaded VCM.

tion voltage. This was done by applying the excitation voltage to the VCM loaded with an ablated μPM having 12 sides. The μPM rotates at the same speed as the VCM since it is attached directly to the rotor. Moreover, the rotational speed (ω_r) of the VCM is directly proportional to the frequency of the excitation signal (f_{ele}) and inversely proportional to the number of rotor poles ($N_r = 8$ in the tested device). It is given by the following equation (2).

The rotational speed of the μRS at various driving voltage amplitudes was calculated and plotted in Figure 11. The maximum speed of the VCM is 2,100 rpm at a peak voltage of 186 V, with the 12-sided laser ablated μPM load. At a particular drive voltage, the μRS can provide a range of rotational speeds by changing the excitation frequency, but the input voltage needs to be increased to attain rotational speeds above that range. This behavior can be explained by considering the fact that, beyond a certain excitation frequency, the available electrical power has to be increased to match the required mechanical power that is increasing with the rotational speed of the motor. The VCM stop operating when the required mechanical power is greater than the supplied electrical power. The electrical power consumed by the μRS and the unloaded VCM (i.e. without an ablated μPM) at different speeds is shown in Figure 12. As expected, at a given rotational speed, the power consumed by the μRS is higher than the power consumed by the unloaded VCM. This is due to the extra load on the rotor. The unloaded VCM can operate at up to 3,300 rpm and consumes a maximal electrical power of 8.6 mW. The maximum power consumed by the μRS is 6.8 mW when operating at a speed of 2,100 rpm.

The frictional torque at the contact point (i.e., dimples) is proportional to the applied normal load [46], [47], and the frictional viscous drag of the micromotor increases with the rotational speed [37], [48]. Additionally, the frictional torque due to the rotor-dimple contact and rotor-central-pin-bearing contact increases quadratically with the applied voltage [48]. Thus, the higher power dissipation of the μRS in comparison to the VCM is due to the addition of the PM resulting in the increase of the normal load and viscous drag. Moreover, the motion dynamics of the micromotor are complex due to
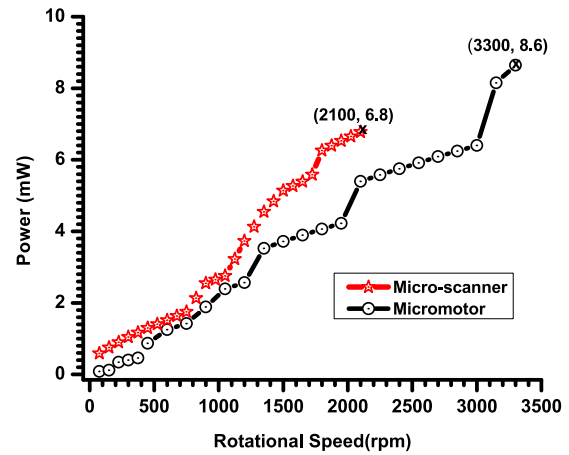
TABLE II
COMPARISON OF THE PROPOSED DEVICE
TO OTHER MEMS SCANNERS

Device type	FoV	Device Dimensions
RBS [54]	$28^\circ \times 31^\circ$	$5.3 \times 5.8 \times 3.0$ mm^3
DMD [53]	48°	10.2×10.2 μm^2
RBS [55]	$45.3^\circ \times 42.6^\circ$	$20 \times 20 \times 16$ mm^3
UDS [56]	30°	$6.75 \times 6.75 \times 2$ mm^3
This work	57.88°	$\mathbf{1.12 \times 1.12 \times 0.83}$ mm^3

RBS stands for resonant bi-directional scanner; UDS stands for uni-directional scanner.

the strong electro-mechanical coupling at various regions that may cause charge accumulation in scratched areas or variations in the fringe fields. Thus, depending on the impact of the coupling effects and the various frictional torques, the power consumption at a particular frequency for a given applied voltage can vary between devices. This could explain the disparity in the power plots of the μRS and the VCM.

C. Optical Characterization

The optical characterization of the μRS was carried-out to measure the scan angle (SA) of the reflected beam, the line scan rate and the scanning frequency. When the μPM rotates, it generates a scan line (SL) of the reflected beam between points A and B on the screen corresponding to the SA, as shown in Figure 13(a) (also labeled in Figure 9(b)). At low excitation frequencies, the μPM rotates slowly and the scan speed is low, thus the laser spot can be traced and captured on the screen. The rotor of the VCM exhibits a small wobbling motion because the electrostatic force continuously pulls it towards the stator poles. However, the rotor sliding motion is halted by the central bearing axis making the rotor trajectory circular. Also, the unbalanced vertical electrostatic forces between the rotor and the stator contribute to the wobbling motion of the rotor. These forces are generated due to the vertical misalignment between the rotor poles and stator poles. The misalignment is approximately 750 nm and it is a

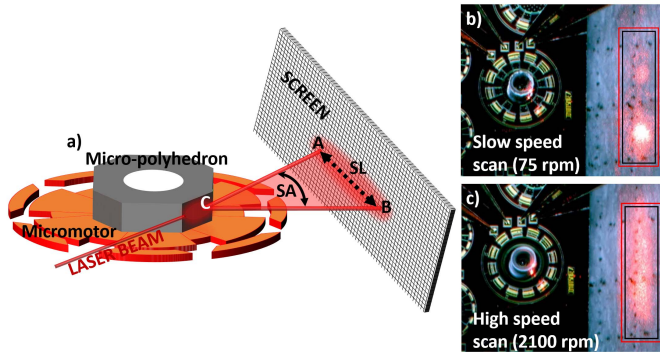| Model (Polygon scanner)	Size (Inscribed circle diameter×Mirror thickness)	Weight	Speed	Power
PD40ERB [11] (Nidac-Copal)	40 mm × 3 mm	200 g	3000-8000 rpm	>12 W
Gecko Four [13] (PLL)	25 mm × 25 mm	190 g	1000-4000 rpm	>6 W
YA90 [12] (Miradatechnology)	20 mm × 3 mm	250 g	1000-6000 rpm	NA
This work	**0.4 mm × 0.4 mm**	**175 μg**	**75-2100 rpm**	**<7 *m*W**

Fig. 13.   a) Schematic illustrating the scanning motion the micro rotary scanner; b) image of the beam on the screen at slow rotational speed (75 rpm); and c) image of the beam on the screen at high rotational speed (2100 rpm).
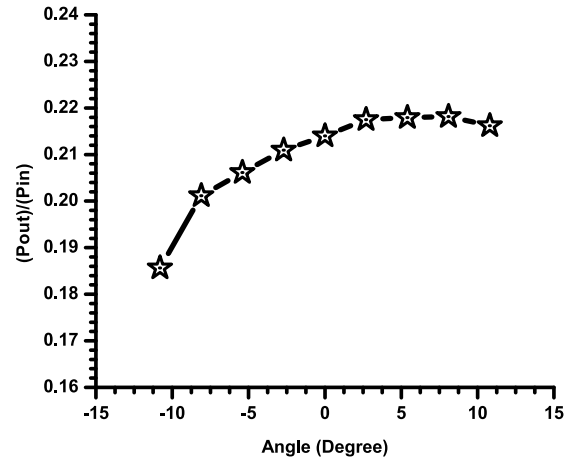

Fig. 14.   The output optical power (P_{out}) across the scan line captured by the photo-detector for a 632 nm laser beam reflected on the μPM and having an input optical power (P_{in}) of 856 μW (−0.68 dBm).

fabrication constraint of the PolyMUMPs process. The impact of the wobbling motion on the scanning motion is that the reflected beam follows a zigzag pattern on the screen, which is clearly visible at low speed (i.e. 75 rpm), and this can be seen in the video file named Slow_Speed_Operation in the supplemental material. At higher frequencies, the rotor is moving very fast (i.e. 2100 rpm), reducing the μRS wobble due to the high inertia of motion. Consequently, the scan pattern of the reflected beam becomes significantly smoother and more linear, as shown in the video file named High_Speed_Operation. Moreover, the zigzag motion of the μPM resulted in the vertical misalignment of the reflected beam by $\approx 6.3°$. The wobbling motion limits the capacity to control the position of the reflected beam, resulting in a beam offset and reduced scanning accuracy. The degraded resolution may induce error in the measurement of the pixels of the radial distance generating a wobbly point cloud for LiDAR applications. Also, it can cause the overlap of scan lines and reduce the image quality for 2-D raster scanning applications. However, the amount of resolution degradation due to the wobbling motion or zig-zag trajectory needs to be evaluated and accessed for each application.

The μRS demonstrated here could be used to implement a 1×N optical switch by placing an array of optical ports at the screen location. For such applications, the optical power transmitted by the μRS to the output ports needs to be determined, and is measured with the optical setup used in the experiment. The 632-nm laser can provide a spot size of 5 μm using a 5X objective with depth of field of 14 μm. The power of the reflected beam was measured using a photo-diode sensor (S120VC from Thorlabs) placed at a distance of 6 cm from the

μRS. The area of the photo-detector is a circle of 9.7 mm in diameter and it cannot cover the entire angular scanning range of the reflected beam. As a result, the output optical power (P_{out}) is measured only across a portion of the SL. Accordingly, the power measurements are reported over a limited range of 22°. Figure 14 shows the ratio of the output power over the input optical power (P_{in}) plotted against the scanning range covered by the photo-detector. The optical power of the incident 632 nm laser beam is 856 μW (−0.68 dBm), and the beam is deflected by the rotating micro-polyhedron onto the photo-detector with an optical output power in the range of 154.08 μW (−8.12 dBm) to 188.32 μW (−7.25 dBm). This yeilds a range for P_{out}/P_{in} from 0.18 to 0.22. No other optical component was used after the beam was reflected from the μRS for experimental simplicity. This is one of the reason for the relatively high optical losses. The collimation of the laser beam could be improved by designing micro-optical elements for the target application. Additionally, during the scanning of the laser beam, the edges at the two ends of the photo-detector truncate the incident beam leading to vignetting, causing a non-uniform optical power distribution along the SL captured by the photo-detector [49].

The major factor responsible for the poor optical efficiency of the μRS is the rough sidewalls of the μPM that result from DRIE of the silicon substrate. This anisotropic etch process is performed by alternating etching and passivation steps in repeated cycles [42]. This results in sidewalls having a scalloped morphology [38], resulting in a rough surface that limits
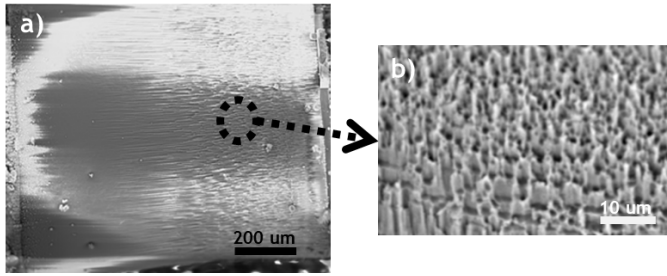
Fig. 15. SEM images of the micro-polygon showing surface morphology. a) Image of the sidewall. b) Zoomed image of the sidewall showing roughness.

the optical performance. The DRIE-induced surface roughness can be seen in the SEM images of the μPM shown in Figure 15. The sidewall roughness causes beam scattering, which reduces the signal-to-noise ratio, and is responsible for the reduced optical efficiency. However, the optical characteristics of the μPM could be improved before it was integrated onto the micromotor by using scallop smoothing techniques [50], [51] that would significantly reduce the scallop depth (up to 90%). This could then be followed by a final step during which a highly reflective thin metal layer would be deposited onto the μPM. While such post-processing of the μPM can enhance the optical efficiency, this work was focused on the demonstration of the chip-scale μRS. The improvement of the optical efficiency of the μPM will be considered in future work.

The angular scanning range (ARS) in degree, the angular scan-rate (ASR) in radian per seconds and the line scan rate (LSR) in line scans per minute for a polygon scanner are given by following equations [52]:

$$ARS = \frac{4\pi}{N} \tag{3}$$

$$ASR = \frac{4\pi \omega_r}{60} \tag{4}$$

$$LSR = \omega_r N \tag{5}$$

where ω_r is the rotational speed of the polygon and N is its number of sides. The experimentally measured scanning range was obtained by measuring the length of the scan line generated on the screen and the distance between the screen and the scanner. Using this method, the μRS presented here covered an angular scanning range of 57.88°, a value that is in good agreement with the calculated value of 60°, stemming from (4). This yields an angular scan rate of 440 radians per second and a maximum scan speed of 25,200 line-scans per minute or 420 line-scans per second. There is a 2.12° variation in the measured scan angle as compared to the scan angle given by the equation due to scattering at the edges of the μPM facet. The wide scanning range of the μRS enables efficient beam steering to distribute the incoming optical signal across a large array of optical ports in switching applications or to scan a wide FoV in ranging applications. In our demonstrator, no significant change in the spot size uniformity was observed during scanning since the theoretical scanning range was limited to 60 degrees because we used a polygon with 12 facets.

However, maintaining a uniform spot over a large angular range would require complex collimating optics. Thus, there is a trade-off between the complexity of the system and the scanning range that it can provide.

V. Discussion

To the best knowledge of the authors, this μRS has the smallest size and highest FoV compared to previous miniaturized MEMS scanners, as shown in table II. The precise integration of the μPM on the VCM make it a well-aligned vertical scanning mirror without the need of additional steps for alignment and positioning. The single pixel of a commercial digital micromirror device (DMD) module offers a smaller footprint than this scanner but the FoV of the pixel is limited to 24°. Moreover, it requires multiple light sources, such as an array of laser diodes, to enhance its FoV in LiDAR type applications [53]. The footprint of the proposed μRS is more than five times smaller than the other scanning modules. In addition, it operates at low power and weighs much less than other modules, making it a highly compact optical scanner.

The μRS proposed is a non-resonant device, while other reported scanners presented in table II are resonant devices. Therefore, a comparison to other commercial rotational polygon scanners is presented in table III, listing footprint, power, speed, and mass. The total dissipated power in commercial systems includes the power required by the polygon motor, driver electronics and encoder. The polygon mirror combined with the motor is the scanning component of a polygon scanner and its footprint is proportional to the dimensions of the motor and the polygon mirror. The size of the polygon mirror is determined by the diameter of the circle inscribed by the polygon and its thickness. Accordingly, Table III uses the inscribed circle diameter (base diameter) and mirror thickness as size metrics in order to compare the footprints of various polygon scanners. We have not considered the dimensions of the motor driving the other scanners presented, as the size would be much larger than that of the device proposed. In the case of the proposed device, the thickness of the mirror is 400 μm (i.e., the thickness of the substrate of the SOI wafer) and the inscribed circle diameter is also 400 μm. The successful integration of the μPM onto the VCM makes the proposed device one of the smallest rotary polygon scanner reported to date. The dimensions of the μPM (height of 400 μm × base diameter of 400 μm) are very small compared to commercial polygon mirrors, which have a height and a base diameter that are larger than 5 mm × 5 mm. The height of the μRS is given by the sum of the μPM substrate thickness, the micromotor substrate thickness and the thickness of the deposited layers. This amounts to 830 μm. Additionally, the mass of the assembled μRS is approximately 175 μg. The overall size of a single μRS is 1.12 mm × 1.12 mm × 0.830 mm, which is more than five-fold smaller than other rotary polygon scanners [11]–[13], [57], [58]. Also, the motors used in commercial polygon-scanners are bigger and heavier than the VCM presented in this work. Combined with the control electronics, the size of a typical polygon-scanner typically

goes beyond 5 mm × 5 mm × 5 mm in size and weighs in the order of hundreds of grams. In addition, a considerable amount of power is required to rotate the larger polygon mirrors, therefore direct current motors are used to meet this requirement. In contrast, the power required to operate the proposed μRS is a few milliwatts, due to the electrostatic operation of the VCM and the small size and mass of the μPM. Along with the supporting optics and electronics components, the commercial polygon scanners presented in table III are widely used in LiDAR modules [14], [59]–[61]. Generally, an array of LiDAR modules is used to increase the scanning angle [62] and are suitable for few applications in spite of their large size and high power consumption. However, these modules pose serious integration and cost challenges for compact systems such as small-scale robots like RoASCH, DASH, HARM, VelociRoACH [63] and micro air vehicles like the RoboBee [64]. With a weight of only 175 μg, the compact scanner presented here is well-suited for chip-scale implementation of low-power LiDAR sensor modules for applications such as drones and miniaturized autonomous vehicles. It also has several other potential applications, including in variable optical attenuators, delay lines for biomedical imaging and chip-scale interferometers.

VI. Conclusion

In this work, an optical μRS comprised of a 12-side μPM integrated onto a VCM was presented. The μRS is implemented through the micro-assembly of the μPM and VCM that are fabricated using low-cost commercial MEMS fabrication processes. The rotary platform consist of a high speed VCM built with the PolyMUMPs surface micromachining process, to enable a low power and compact rotational platform, while the μPM was fabricated using the PiezoMUMPs bulk micromachining process, to provide a large reflective surface for low optical power losses. It was post-processed to reduce its mass to enable rotary motion.

The device demonstrated a high scan rate, large scan angle and low power consumption. This miniaturized polygon scanner has a small footprint and can be integrated in chip-scale subsystems. It is well-suited for applications where mass, compactness, power consumption and scanning speed are important. To the best of the authors' knowledge, this work reports the first micro-scale high-speed rotary-scanner, and paves the way for the investigation of system applications that can take advantage of its unique properties. For instance, the μRS could be well-suited to systems such as advanced driving assistance systems, LiDARs for robots and drones, endoscopic imagers, and optical switches, potentially enabling a significant miniaturization and cost reduction of these systems.

Acknowledgment

References

[1] S. T. S. Hölmstrom, U. Baran, and H. Urey, "MEMS laser scanners: A review," *J. Microelectromech. Syst.*, vol. 23, no. 2, pp. 259–275, Apr. 2014.

[2] Y. Li, H. M. Huang, G. Burgio, W. Heath, and W. M. Lee, "Dynamic control over field of view in polygon mirror-based laser scanning multiphoton microscope," in *Proc. Opt. Life Sci. Congr.* Washington, DC, USA: Optical Society of America, 2017, paper BoTu3A.2. [Online]. Available: http://www.osapublishing.org/abstract.cfm?URI=BODA-2017-BoTu3A.2

[3] T. Wang, C. Zhang, A. Aleksov, I. Salama, and A. Kar, "Effect of large deflection angle on the laser intensity profile produced by acousto-optic deflector scanners in high precision manufacturing," *J. Laser Appl.*, vol. 28, no. 1, Feb. 2016, Art. no. 012012, doi: 10.2351/1.4937174.

[4] A. Li, W. Sun, W. Yi, and Q. Zuo, "Investigation of beam steering performances in rotation Risley-prism scanner," *Opt. Exp.*, vol. 24, no. 12, pp. 12840–12850, Jun. 2016. [Online]. Available: http://www.opticsexpress.org/abstract.cfm?URI=oe-24-12-12840

[5] H. W. Yoo, S. Ito, and G. Schitter, "High speed laser scanning microscopy by iterative learning control of a galvanometer scanner," *Control Eng. Pract.*, vol. 50, pp. 12–21, May 2016. [Online]. Available: http://www.sciencedirect.com/science/article/pii/S09670 6611630020X

[6] A. Harrison and P. Newman, "High quality 3D laser ranging under general vehicle motion," in *Proc. IEEE Int. Conf. Robot. Autom.*, May 2008, pp. 7–12.

[7] R. Thakur, "Scanning LiDAR in advanced driver assistance systems and beyond: Building a road map for next-generation LiDAR technology," *IEEE Consum. Electron. Mag.*, vol. 5, no. 3, pp. 48–54, Jul. 2016.

[8] J. Hecht, "LiDAR for self-driving cars," *Opt. Photon. News*, vol. 29, no. 1, pp. 26–33, 2018. [Online]. Available: https://www.osa-opn.org/home/articles/volume_29/january_2018/features/lidar_for_self-driving_cars/

[9] F. Moosmann and C. Stiller, "Velodyne SLAM," in *Proc. IEEE Intell. Vehicles Symp. (IV)*, Jun. 2011, pp. 393–398.

[10] Z. Gong, J. Li, Z. Luo, C. Wen, C. Wang, and J. Zelek, "Mapping and semantic modeling of underground parking lots using a backpack LiDAR system," *IEEE Trans. Intell. Transp. Syst.*, vol. 22, no. 2, pp. 734–746, Feb. 2021.

[11] Nidec-Copal-Electronics. (2020). *Polygon Laser Scanner*. [Online]. Available: https://www.nidec-copal-electronics.com/e/catalog/polygon-laser-scanner/pd60ea.pdf

[12] Miradatechnologies. (2018). *Polygon Laser Scanner*. [Online]. Available: https://miradatechnologies.com/wp-content/uploads/2019/11/2019_1104_Mirada_BE_Series_Product_Data_Sheet_PRELIMINARY.pdf

[13] PLL. (2019). *Gecko Four LiDAR Scanner With 25 mm Aperture*. [Online]. Available: https://precisionlaserscanning.com/wp-content/uploads/2019/09/GECKO-FOUR-BROCHURE-13SEP19.pdf

[14] H. Weber. (2018). *Sick AG White Paper*. [Online]. Available: https://cdn.sick.com/media/docs/3/63/963/Whitepaper_LiDAR_en_IM0079963.PDF

[15] S. Chung, H. Abediasl, and H. Hashemi, "A monolithically integrated large-scale optical phased array in silicon-on-insulator CMOS," *IEEE J. Solid-State Circuits*, vol. 53, no. 1, pp. 275–296, Jan. 2018.

[16] C.-P. Hsu *et al.*, "A review and perspective on optical phased array for automotive LiDAR," *IEEE J. Sel. Topics Quantum Electron.*, vol. 27, no. 1, pp. 1–16, Jan./Feb. 2021.

[17] M. Hafez, T. C. Sidler, R. P. Salathé, G. L. M. Jansen, and J. C. Compter, "Design, simulations and experimental investigations of a compact single mirror tip/tilt laser scanner," *Mechatronics*, vol. 10, no. 7, pp. 741–760, Oct. 2000. [Online]. Available: http://www.sciencedirect.com/science/article/pii/S0957415899000938

[18] Y.-Y. Ji, B. H. So, and D. Y. Kim, "High-speed time-domain characterization method for polygon scanners," *Measurement*, vol. 135, pp. 278–286, Mar. 2019. [Online]. Available: http://www.sciencedirect.com/science/article/pii/S0263224118310935

[19] P. J. Chiang *et al.*, "Printer and scanner forensics," *IEEE Signal Process. Mag.*, vol. 26, no. 2, pp. 72–83, Mar. 2009.

[20] R. De Loor, L. Penning, and R. Slagle, "Polygon laser scanning," *Laser Technik J.*, vol. 11, no. 3, pp. 32–34, Jun. 2014. [Online]. Available: https://onlinelibrary.wiley.com/doi/abs/10.1002/latj.201400033

[21] S. H. Yun, C. Boudoux, G. J. Tearney, and B. E. Bouma, "High-speed wavelength-swept semiconductor laser with a polygon-scanner-based wavelength filter," *Opt. Lett.*, vol. 28, no. 20, pp. 1981–1983, Oct. 2003. [Online]. Available: http://ol.osa.org/abstract.cfm?URI=ol-28-20-1981

[22] W. Y. Oh, S. H. Yun, G. J. Tearney, and B. E. Bouma, "115 kHz tuning repetition rate ultrahigh-speed wavelength-swept semiconductor laser," *Opt. Lett.*, vol. 30, no. 23, pp. 3159–3161, Dec. 2005. [Online]. Available: http://ol.osa.org/abstract.cfm?URI=ol-30-23-3159

[23] V.-F. Duma and A. G. Podoleanu, "Polygon mirror scanners in biomedical imaging: A review," *Proc. SPIE*, vol. 8621, pp. 175–183, Mar. 2013, doi: 10.1117/12.2005065.

[24] B.-K. Luo, A. He, J. Lu, and X.-W. Ni, "Studies on nonlinearity of rotating mirror scanning in laser imaging radar," *Proc. SPIE*, vol. 2271, pp. 109–114, Sep. 1994, doi: 10.1117/12.188144.

[25] D. Wang, C. Watkins, and H. Xie, "MEMS mirrors for LiDAR: A review," *Micromachines*, vol. 11, no. 5, p. 456, Apr. 2020.

[26] A. R. Cho et al., "Electromagnetic biaxial microscanner with mechanical amplification at resonance," *Opt. Exp.*, vol. 23, no. 13, pp. 16792–16802, Jun. 2015. [Online]. Available: http://www.opticsexpress.org/abstract.cfm?URI=oe-23-13-16792

[27] Y. M. Sabry, D. Khalil, B. Saadany, and T. Bourouina, "Integrated wide-angle scanner based on translating a curved mirror of acylindrical shape," *Opt. Exp.*, vol. 21, pp. 13906–13916, Jun. 2013. [Online]. Available: http://opg.optica.org/oe/abstract.cfm?URI=oe-21-12-13906

[28] H. Toshiyoshi, G. D. J. Su, J. LaCosse, and M. C. Wu, "A surface micromachined optical scanner array using photoresist lenses fabricated by a thermal reflow process," *J. Lightw. Technol.*, vol. 21, no. 7, pp. 1700–1708, Jul. 2003.

[29] J. Brière, P.-O. Beaulieu, M. Saidani, F. Nabki, and M. Menard, "Rotational MEMS mirror with latching arm for silicon photonics," *Proc. SPIE*, vol. 9375, pp. 20–26, Feb. 2015, doi: 10.1117/12.2077033.

[30] A. A. Yasseen, J. N. Mitchell, D. A. Smith, and M. Mehregany, "High-aspect-ratio rotary polygon micromotor scanners," *Sens. Actuators A, Phys.*, vol. 77, no. 1, pp. 73–79, Sep. 1999. [Online]. Available: http://www.sciencedirect.com/science/article/pii/S0924424799001879

[31] C.-C. Tu, K. Fanchiang, and C.-H. Liu, "1×N rotary vertical micromirror for optical switching applications," *Proc. SPIE*, vol. 5719, pp. 14–22, Jan. 2005, doi: 10.1117/12.589810.

[32] M. A. Basha, "3D rotating octagonal micromirror optical scanner: Design, fabrication, and assembly," *Proc. SPIE*, vol. 8428, pp. 275–282, May 2012, doi: 10.1117/12.924282.

[33] A. Gour, M. Ménard, and F. Nabki, "Low-friction, high-speed rotary 3-phase micromotor using the PolyMUMPS process," *J. Microelectromech. Syst.*, vol. 29, no. 4, pp. 532–543, Aug. 2020.

[34] I. Dufour, E. Sarraute, and A. Abbas, "Optimization of the geometry of electrostatic micromotors using only analytical equations," *J. Micromech. Microeng.*, vol. 6, no. 1, pp. 108–111, Mar. 1996.

[35] N. Ghalichechian, A. Modafe, M. I. Beyaz, and R. Ghodssi, "Design, fabrication, and characterization of a rotary micromotor supported on microball bearings," *J. Microelectromech. Syst.*, vol. 17, no. 3, pp. 632–642, Jun. 2008.

[36] F. T. Han, Q. P. Wu, and L. Wang, "Experimental study of a variable-capacitance micromotor with electrostatic suspension," *J. Micromech. Microeng.*, vol. 20, no. 11, Oct. 2010, Art. no. 115034.

[37] U. Beerschwinger, R. L. Reuben, and S. J. Yang, "Frictional study of micromotor bearings," *Sens. Actuators A, Phys.*, vol. 63, no. 3, pp. 229–241, Dec. 1997.

[38] D. C. Miller, B. L. Boyce, M. T. Dugger, T. E. Buchheit, and K. Gall, "Characteristics of a commercially available silicon-on-insulator MEMS material," *Sens. Actuators A, Phys.*, vol. 138, no. 1, pp. 130–144, Apr. 2007.

[39] W. Zhang, G. Meng, and H. Li, "Electrostatic micromotor and its reliability," *Microelectron. Rel.*, vol. 45, nos. 7–8, pp. 1230–1242, Jul. 2005.

[40] A. Cowen, B. Hardy, R. Mahadevan, and S. Wilcenski, *PolyMUMPs Design Handbook*, vol. 13. Durham, NC, USA: MEMSCAP, 2011.

[41] A. Cowen, G. Hames, K. Glukh, and B. Hardy, *PiezoMUMPs Design Handbook*. Duham, NC, USA: MEMSCAP, 2013.

[42] F. Laermer and A. Schilp, "Method of anisotropically etching silicon," U.S. Patent 5 501 893 A, Mar. 6, 1996.

[43] W. H. Juan and S. W. Pang, "Controlling sidewall smoothness for micromachined Si mirrors and lenses," *J. Vac. Sci. Technol. B, Microelectron. Nanometer Struct. Process., Meas., Phenomena*, vol. 14, no. 6, pp. 4080–4084, 1996.

[44] I.-H. Song, Y.-A. Peter, and M. Meunier, "Smoothing dry-etched microstructure sidewalls using focused ion beam milling for optical applications," *J. Micromech. Microeng.*, vol. 17, no. 8, pp. 1593–1597, Jul. 2007.

[45] P. Svasek, E. Svasek, B. Lendl, and M. Vellekoop, "Fabrication of miniaturized fluidic devices using SU-8 based lithography and low temperature wafer bonding," *Sens. Actuators A, Phys.*, vol. 115, nos. 2–3, pp. 591–599, Sep. 2004. [Online]. Available: https://www.sciencedirect.com/science/article/pii/S0924424704002389

[46] J. A. Williams, "Friction and wear of rotating pivots in MEMS and other small scale devices," *Wear*, vol. 251, nos. 1–12, pp. 965–972, Oct. 2001. [Online]. Available: https://www.sciencedirect.com/science/article/pii/S0043164801007207

[47] W.-M. Zhang and G. Meng, "Friction and wear study of the hemispherical rotor bushing in a variable capacitance micromotor," *Microsyst. Technol.*, vol. 12, no. 4, pp. 283–292, Mar. 2006.

[48] S. F. Bart, M. Mehregany, L. S. Tavrow, J. H. Lang, and S. D. Senturia, "Electric micromotor dynamics," *IEEE Trans. Electron Devices*, vol. 39, no. 3, pp. 566–575, Mar. 1992.

[49] Y. Zhang and L. Chen, "Vignetting and the scan duty cycle of dual-beam scanning field by polygon scanners," *Proc. SPIE*, vol. 3963, pp. 544–550, 1999, doi: 10.1117/12.373436.

[50] Z. A. S. Mohammed, M. A. S. Olimpo, D. P. Poenar, and S. Aditya, "Smoothening of scalloped DRIE trench walls," *Mater. Sci. Semicond. Process.*, vol. 63, pp. 83–89, Jun. 2017.

[51] J. S. Park et al., "Low-temperature smoothing method of scalloped DRIE trench by post-dry etching process based on SF₆ plasma," *Micro Nano Syst. Lett.*, vol. 8, no. 1, p. 14, Aug. 2020.

[52] E. Erdelyi and G. A. Rynkowski, "Motors and controllers (drivers) for high-performance polygonal scanners," in *Handbook of Optical and Laser Scanning*, G. F. Marshall and G. E. Stutz, Eds. Boca Raton, FL, USA: CRC Press, 2013, pp. 282–318.

[53] B. Smith, B. Hellman, A. Gin, A. Espinoza, and Y. Takashima, "Single chip LiDAR with discrete beam steering by digital micromirror device," *Opt. Exp.*, vol. 25, no. 13, pp. 14732–14745, Jun. 2017. [Online]. Available: http://www.opticsexpress.org/abstract.cfm?URI=oe-25-13-14732

[54] D. Wang, S. J. Koppal, and H. Xie, "A monolithic forward-view MEMS laser scanner with decoupled raster scanning and enlarged scanning angle for micro LiDAR applications," *J. Microelectromech. Syst.*, vol. 29, no. 5, pp. 996–1001, Oct. 2020.

[55] L. Ye, G. Zhang, Z. You, and C. Zhang, "A 2D resonant MEMS scanner with an ultra-compact wedge-like multiplied angle amplification for miniature LiDAR application," in *Proc. IEEE SENSORS*, Oct. 2016, pp. 1–3.

[56] T. Pensala et al., "Wobbling mode AlN-piezo-MEMS mirror enabling 360-degree field of view LiDAR for automotive applications," in *Proc. IEEE Int. Ultrason. Symp. (IUS)*, Oct. 2019, pp. 1977–1980.

[57] Nanophorm. (2018). *Polygon Scanners*. [Online]. Available: https://http://nanophorm.com/services/precision-machining-and-diamond-cutting/products/polygon-scanners/

[58] Cambridge Technology. (2020). *Polygon Laser Scanner*. [Online]. Available: https://camtechfiles.s3-us-west-2.amazonaws.com/s3fs-public/Datasheet%20-%20MotorPolygonAssemblies%28DS00025%29_2018_v4.pdf

[59] C. I. Rablau, "LiDAR: A new self-driving vehicle for introducing optics to broader engineering and non-engineering audiences," *Proc. SPIE*, vol. 5, no. 3, pp. 48–54, 2019.

[60] Velodyne. (2019). *VLP-16 Datasheet*. [Online]. Available: https://www.mapix.com/wp-content/uploads/2018/07/63-9229_Rev-H_Puck-_Datasheet_Web-1.pdf

[61] SICK. (2019). *LMS-4000 Datasheet*. [Online]. Available: https://cdn.sickcn.com/media/familyoverview/1/51/751/familyOverview_LMS4000_g474751_en.pdf

[62] S. Zeng, "A tracking system of multiple LiDAR sensors using scan point matching," *IEEE Trans. Veh. Technol.*, vol. 62, no. 6, pp. 2413–2420, Jul. 2013.

[63] T.-Y. Kim, C. Kim, S.-H. Kim, and G.-P. Jung, "MutBug: A lightweight and compact crawling robot that can run on both sides," *IEEE Robot. Autom. Lett.*, vol. 4, no. 2, pp. 1409–1415, Apr. 2019.

[64] T. S. Clawson, S. Ferrari, S. B. Fuller, and R. J. Wood, "Spiking neural network (SNN) control of a flapping insect-scale robot," in *Proc. IEEE 55th Conf. Decis. Control (CDC)*, Dec. 2016, pp. 3381–3388.

Amit Gour (Member, IEEE) received the B.Eng. degree in electronics and communication engineering from Devi Ahilya Vishwavidyalaya, Indore, India, in 2009, the M.Tech. degree in electrical engineering from the Indian Institute of Technology Bombay, Mumbai, India, in 2012, and the Ph.D. degree in electrical engineering from the École de Technologie Supérieure, Montreal, Canada, in 2021. In 2012, he joined ST-Ericsson, Bengaluru, India, as an ASIC Physical Design Engineer for the development of LTE modems using FD-SOI technology. In 2014, he joined the eCPU Department, TSMC, Hsinchu, Taiwan, as an ASIC Engineer, adding to the implementation of HP-ASICs for advance nodes. He is currently working on the digital implementation of the UWB transceiver at SPARK Microsystems, Montreal. His research interests include MEMS design and fabrication, photonic design, and VLSI design.

Michaël Ménard (Member, IEEE) was born in Quebec, QC, Canada. He received the B.Eng. and Ph.D. degrees in electrical engineering from McGill University, Montreal, QC, Canada, in 2002 and 2009, respectively. At McGill University, he worked on the design and implementation of novel devices for optical telecommunication applications, including spatial formatting in dense wavelength division multiplexer and broadband high-density electro-optical space switches in III–V waveguides. From 2009 to 2011, he was a Post-Doctoral Fellow with the Cornell Nanophotonics Group under the supervision of Prof. Michal Lipson. At Cornell University, he investigated broadband wavelength conversion with silicon waveguides for fiber and free space telecommunication. In June 2011, he joined the Microelectronic Program at UQAM until September 2021 when he started to work with the Department of Electrical Engineering, École de Technologie Supérieure. He is an active member of NanoQAM, the research center on nanomaterials and energy. He jointly manages the Microtechnology and Microsystems Laboratory. In 2019, he was a Visiting Research with the Department of Applied Physics, University of Campinas, São Paulo, Brazil. He holds or has held financial support from the Microsystems Strategic Alliance of Quebec (ReSMiQ), the Center for Optics, Photonics, and Lasers (COPL), the Quebec Fund for Research in Nature and Technology (FRQNT), Prompt Québec, PRIMA Québec, and the Natural Sciences and Engineering Research Council of Canada (NSERC). He has published over 80 publications, and holds five issued patents and three pending patent applications. His research interests include integrated optics, silicon photonics, nonlinear optics, micro-opto-electro-mechanical systems (MOEMS), optomechanics, and microfabrication. He is a member of the Quebec Order of Engineers.

Frederic Nabki (Member, IEEE) received the B.Eng. degree (Hons.) in electrical engineering and the Ph.D. degree in electrical engineering from McGill University, Montreal, QC, Canada, in 2003 and 2010, respectively. In 2008, he joined the Université du Québec à Montréal (UQAM), Montreal, where he was an Associate Professor in microelectronics engineering. In 2016, he joined the École de Technologie Supérieure, Montreal, where he is currently a Full Professor with the Department of Electrical Engineering. He holds or has held financial support from the Microsystems Strategic Alliance of Quebec, the Quebec Fund for Research in Nature and Technology, the Natural Sciences and Engineering Research Council of Canada, and the Canada Foundation for Innovation. He has authored two book chapters and over 150 publications. He holds 44 issued patents on applications related to MEMS, ICs, and CMOS/MEMS monolithic integration. His research interests include microelectromechanical systems (MEMS) and RF/analog microelectronics, specifically focusing on the creation of next-generation MEMS processes using advanced materials; the integration of MEMS devices with CMOS systems; the modeling of MEMS devices; and the design of CMOS phase-locked loops, ultra-wideband transceivers, and MEMS interface circuits. He is currently a member of the Quebec Order of Engineers. He was a recipient of the Governor General of Canada's Academic Bronze Medal, the IEEE Canada J. J. Archambault Eastern Canada Medal, and the UQAM Faculty of Science Early Career Research Award. He has served as the Secretary and the Treasurer for the Montreal Section of the IEEE. He was the Founder and the Associate Director of the Institutional Research Centre on the Co-Design and Fabrication of Microsystems, UQAM; and jointly manages the Microtechnology and Microsystems Laboratory.